Individual activator and repressor transcription factors induce global changes in chromatin mobility

Haitham A. Shaban[1, 2, *] and David M. Suter[1, *]

1: Institute of Bioengineering, Ecole Polytechnique Fédérale de Lausanne (EPFL), 1025 Lausanne, Switzerland.2: Spectroscopy Department, Institute of Physics Research, National Research Centre, Dokki, 12622 Cairo, Egypt.

*: To whom correspondence should be addressed: Haitham A. Shaban. Email:haitham.shaban@epfl.ch and David Suter Email: david.suter@epfl.ch

The control of eukaryotic gene expression is intimately connected to highly dynamic chromatin structures. Gene regulation relies on activator and repressor transcription factors (TFs) that induce local chromatin opening and closing. Yet how nucleus-wide chromatin structures respond dynamically to the activity of specific TFs remains unclear. Here we asked how TFs with opposite effects on modulating local chromatin accessibility impact nucleus-wide chromatin dynamics in living cells. We combine High-resolution Diffusion mapping (Hi-D) and Dense Flow reConstruction and Correlation (DFCC) to obtain an imaging-based, nanometer-scale analysis of local diffusion processes and long-range coordinated movements of both chromatin and TFs in live cells. We show that expression of individual activator and repressor TFs increases nucleus-wide chromatin mobility and induces opposite coherent chromatin motions at the micron scale. Our quantitative analysis thus reveals the broad and differential impact of TFs opening and closing chromatin in nucleus-wide chromatin dynamics.

Introduction

In eukaryotes, genomic DNA is packaged into nucleosomes that are organized in a 3D structure called chromatin. Spatial organization of chromatin is defined by short- and long-range interactions, creating a hierarchy of structural elements, the most prominent ones being DNA loops, topologically associated domains, and A/B compartments (*1*, *2*). Active and inactive regions of the genome appear spatially separated, while co-regulated genes are often juxtaposed within the same topological domain (*3*). These hierarchically organized structures are highly dynamic to form and disrupt over different spatial and temporal scales (*4*). Dynamic changes in chromatin structures both regulate and depend on nuclear processes (*5*). Chromatin dynamics were also reported to reflect the degree of DNA accessibility for different transcriptional states (*6*). Remarkably, characteristic chromatin motions could be used to define the 3D topological enhancer-promoter conformations of both actively and inactively transcribed states (*7*). The interplay between long-range chromatin structure and dynamics was proposed to grant access to trans-acting factors to genome regions within dense chromatin structures that display coherent motions (*8*, *9*). This also implies that transcriptional regulators have to achieve their highly spatially and temporally-coordinated interactions (*5*) within an ever-shifting landscape of chromatin structures. How transcriptional regulators themselves modulate local and global chromatin movements is unknown.

The dynamic regulation of chromatin into a nucleosome-sparse (open) or dense (closed) state is initiated by TFs classified into transcriptional activators or repressors, respectively (*6*, *10*). TFs that open chromatin (also called pioneer TFs) act by binding and recruiting chromatin remodelers to displace nucleosomes (*11*). This allows creating a permissive state for the subsequent binding of co-factors required for transcriptional activation (*12*). This ability to shape the chromatin landscape allows pioneer TFs to reprogram entire transcriptional networks and thereby control cell fate decisions (*13*). The second category of TFs acts as transcriptional repressors to shut down transcription (*14*). This generally involves the recruitment of histone modifiers and chromatin remodelers to convert chromatin into a closed-form (*6*, *15*). The regulation of chromatin accessibility is a highly dynamic process, as evidenced by the requirement for continuous activity of the Oct4 TF (*16*) and the BAF chromatin remodeler complex (*15*, *17*) to maintain a locally open chromatin state. Repressive histone modifications are also proposed to be highly dynamic to acutely follow pulses of repression (*18*). How nucleus-wide chromatin structures respond dynamically to a specific TF, and whether this response relies on long-range coordinated motions and TF functions are still undefined.

Single-particle tracking (SPT) methods have been used to study dynamic TF-DNA interactions and to assess the role of TFs in shaping the chromatin mobility landscape in living eukaryotic cells (*19*–*25*). Most of these studies showed that the residence time of DNA-bound TFs affects the temporal expression patterns of transcription (*19*, *23*, *24*) and the spatial organization of chromatin in live cells (*20*, *22*). This shows the importance of residence times as a biophysical characteristic for regulating transcriptional activity and genome organization. A new analytical approach allowing to study the dynamic pioneer TF-chromatin interactions showed that chromatin mobility itself can directly influence the impact of pioneer TFs on gene expression (*26*). So far, the high spatio-temporal mobility analysis of local chromatin organization in living cells has mostly relied on fluorescent labelling of specific genomic sites, which can be spatially resolved and tracked over time using SPT (*27*, *28*). As an alternative approach for imaging sparsely-labelled nucleosomes over the whole nucleus, super-resolution imaging of the H2B histone was combined with SPT to visualize and track chromatin domains in living cells (*26*, *29*). These methods, however, apply one motion model for diffusion characterization that results in an incomplete understanding of the physical mechanisms underlying chromatin motions (*30*). In addition, these are limited to sparse single loci analysis, and thus lack information about neighboring chromatin sequences and long-range correlations of chromatin movements.

We recently introduced two imaging techniques to overcome the limitations of SPT approaches. First, Dense Flow reConstruction and Correlation (DFCC) quantifies nucleus-wide, spatiotemporally correlated motions of chromatin and other nuclear proteins with nanometer precision in single live cells (*31*). Second, high-resolution diffusion mapping (Hi-D) quantifies local diffusion processes and spatially maps the biophysical properties of chromatin and nuclear protein diffusion over the entire nucleus (*32*). Here, we combine Hi-D and DFCC to allow for nucleus-wide characterization of local diffusion processes and long-range coordinated movements of chromatin and TFs with nanometer resolution in mammalian cells. We chose one pioneer (CDX2) and one repressor TF(SIX6) to study the large-scale alterations of chromatin dynamics caused by local chromatin opening or closing. The choice for these TFs stems from our previous finding that expression of CDX2 and SIX6 in NIH-3T3 cells induces chromatin opening and closing at thousands of genomic loci, respectively (*33*). CDX2 plays a key role in regulating the identity of various cell types such as the trophectoderm (*34*) and in the intestine (*35*), while SIX6 is involved in eye development (*36*). We discover that CDX2 and SIX6 dramatically alter nucleus-wide chromatin dynamics and have an opposite impact on coherent chromatin motions at the micron scale. We also assess TF diffusivity in this context; we find that CDX2 and SIX6 display contrasted diffusive behaviors but identical

coherent motions. Our study thus establishes the impact of TFs in shaping long-range chromatin organization and global genome mobility in living cells.

Results

Genome-wide characterization of diffusion processes and long-range correlated motions at nanoscale resolution

To image chromatin in single living cells, we use stable NIH-3T3 cell lines expressing TFs fused to the red fluorescent protein mCherry. Time-lapse spinning disk confocal imaging of 200 frames (6.6 frames per second) for both H2B and TF was acquired (Figure 1A). To access the local diffusion processes of the H2B histone and their coordinated motions over the entire nucleus, we combined Hi-D (*32*) and DFCC (*31*). Both Hi-D and DFCC leverage the Optical Flow (OF) method as the first analysis step to estimate the motion of fluorescently labelled nuclear proteins from time-lapse images with nanoscale precision. DFCC spatially and temporally correlates the flow fields of chromatin motion for both magnitude and direction in a color-coded 2D heat map (Figure 1B). The results yield spatially averaged correlation curves that provide correlation lengths, a quantity representing the extent to which motions are correlated in their direction and magnitude (Figure 1C, D). DFCC analysis showed that chromatin of fibroblast cells exhibits coherent motions with a micron-scale correlation length for both direction and magnitude (Figure 1C, D). These results are consistent with those obtained on human cancer cells (*31*).

Hi-D uses the same flow fields estimated by the OF method for DFCC to integrate trajectories of the displacements over time, from which the Mean Square Displacement (MSD) can be calculated. To spatially resolve the characteristics and heterogeneity of nucleus-wide chromatin motions, Hi-D applies five motion models that underlie the local diffusion process and classifies the best-fitted type of motion for each trajectory by using a Bayesian inference approach (Methods). Considering only the trajectories from chromatin pixels over the whole nucleus, approximately 7000 trajectories (over 199 time points) were analyzed for each nucleus. The applied motion models are i) Free (Brownian) diffusion (D; unrestricted arbitrary molecular motion), ii) Anomalous diffusion (DA; molecular motions that are physically constrained, for example by the presence of obstacles or transient binding events), iii) Directed motion involving a drift velocity (V), iv) Free diffusion with directed motion (DV) and v) Anomalous diffusion with directed motion (DAV, which may result from molecular motor-driven transport). Although the fitting of the five motion models gives different physical parameters, we show only the diffusion constant because it is represented in all five models and is a common biophysical characteristic for histones and TF motions (Figure 1E). Note that the

motion classification provides not only the physical model underlying this motion but also the switching between motion types for different genomic conditions. To categorize the heterogeneous distribution and degree of diffusivity across the entire nucleus, diffusion constant values were represented in a histogram that was deconvolved into discrete subpopulations using a general mixture model (GMM) (Figure 1F) (methods). The spatial distribution of the preferred models for each trajectory can be represented as a color-coded 2D heat map of the entire nucleus (Figure 1G). The percentage of the selected motion models is represented in a Pie chart (Figure 1H). The Hi-D analysis exhibited the chromatin motion heterogeneity of the NIH-3T3 cell line with four selected model motions out of five. Using the GMM, the distribution of diffusion constants was deconvolved into three populations representing slow, intermediate, and fast diffusion regimes.

Altogether, the combination of Hi-D and DFCC methods allows obtaining a spatially resolved, genome-wide analysis of local diffusion processes with the classification of the motion type, as well as heterogeneity and quantification of long-range correlated motions of chromatin.

TFs regulating chromatin accessibility induce a micron-scale coherence in nucleosome dynamics

To study chromatin dynamics in response to the activity of TFs in opening and closing chromatin, we took advantage of a previous study from our laboratory that quantified the impact of different TFs on chromatin accessibility (*33*). We had engineered doxycycline (dox)-inducible NIH-3T3 cell lines to acutely overexpress specific TFs fused to the YPet fluorescent protein. We then performed ChIP-seq and ATAC-seq after dox induction to measure TF-induced changes in chromatin accessibility. We found that CDX2 and SIX6 had a particularly broad impact on chromatin accessibility, opening and closing many regions, respectively (Figure. 2A). We thus decided to use these cell lines to study the dynamic response of chromatin to a chromatin opener (CDX2) and closer (SIX6). Also note that these cell lines had been engineered to express the H2B histone fused to mCherry, thereby allowing for visualizing nucleosomes by microscopy. These cell lines will be referred to as iCDX2 and iSIX6 in the manuscript. We seeded the iCDX2 and iSIX6 cell lines in the presence or absence of doxycycline. Live cell imaging of H2B-mCherry, before and after the overexpression of both CDX2 and SIX6 TF was performed using spinning disk confocal microscopy for 200 frames with 150 ms acquisition.

We then used Hi-D to assess changes in the global chromatin mobility response to CDX2 and SIX6. To ensure that the analyzed nuclei are approximately in the same cell cycle phase, only nuclei with similar sizes were analyzed. Of note, 20 analyzed nuclei per condition means that

about 1.4 x 10^6 of virtual trajectories over 199 time points (on average 7000 trajectories per nucleus) were analyzed. To ensure that changes in dynamic properties are only due to the expression of either CDX2 or SIX6, we used a cell line constitutively expressing the reverse tetracycline transactivator (rtTA3G) only as a control. Our analysis showed no significant differences between the calculated parameters in the presence or absence of dox in the control cell line (Supplementary Figure 1). In contrast, the overexpression of CDX2 or SIX6 induced large changes in chromatin mobility at the whole nucleus scale (Figure 2B, C). The diffusion constants (*D*) for the three populations of H2B in response to CDX2 were significantly increased. We also found alterations in the fraction of trajectories belonging to different motion models underlying these mobilities (Figure 2B). The change in motion models underlying H2B diffusivity in response to Dox was mainly represented by a decrease in anomalous diffusion (DA) and a slight increase in directed motion (DAV) (Figure 2B: bottom panels). Interestingly, *D* values for the three populations of H2B in response to SIX6 for closing chromatin were also significantly increased (Figure 2C). In contrast to CDX2, the motion models describing chromatin diffusivity due to SIX6 expression showed an increased DA and a decrease in DAV motion models (Figure 2C: bottom panels). The increase in DA diffusion in closed chromatin is suggestive of altered DNA-protein interactions and accumulated local concentration of nuclear proteins in a dense chromatin region (*37*), and vice versa for the decrease in DA diffusion.

We then applied DFCC to explore whether the dynamic response of chromatin relies on long-range coordinated motions. The magnitude and direction of the correlation length of H2B movements were determined in the presence or absence of dox (Figure 2D, E). The expression of CDX2 induced a two-fold increase in the correlation length magnitude ($\xi \approx 2$ µm) of H2B motions (Figure 2D) but no change in the directional correlation. In contrast, SIX6 markedly decreased the magnitudinal and directional correlation length of chromatin (Figure 2E). These results are in accordance with the fact that nucleosomes of compact chromatin domains (transcriptionally inactive) move coherently (*29*) with shorter correlation length, in comparison to open chromatin domains (transcriptionally active) (*31*). In conclusion, the expression of an individual TF that either opens or closes chromatin induces an increase in chromatin mobility over a long-range of coordinated movements at the micron scale.

CDX2 and SIX6 induce progressive alterations in coherent chromatin motions

To further explore the dynamic relationship between TF overexpression and chromatin motions, we measured chromatin dynamics at different time points (6, 12, 24 hours) after induction of CDX2 and SIX6 expression. First, we determined the temporal dynamics of TF

concentrations after dox induction. Live cell analysis of CDX2-YPet and SIX6-YPet showed that their expression was already maximized after 6 hours of dox treatment (Figure 3A). This ensures that changes in chromatin dynamics between different time points are not simply caused by a gradual increase of TF concentration, but rather reflect the dynamics of downstream events.

The different dox incubation times impacted global chromatin mobility with similar increases in *D* values for the three populations (Figure 3B, C). The comparison of diffusivity between the different expression times for both CDX2 and SIX6 showed no significant changes (Supplementary Figure 2). This suggests that global chromatin mobility changes are responding to the activity of CDX2 and SIX6 within a few hours. Next, we determined how the duration of TF overexpression impacts coherent movements of histones for opening and closing chromatin. Interestingly, the magnitudinal correlation length of histone motions progressively increased with time upon CDX2 overexpression (Figure 3D), with the same directional correlation length for all conditions (Figure 3F). However, in the case of SIX6 overexpression, the directional correlation length was already maximally decreased after 6 hours of dox incubation (Figure 3E), while the magnitudinal correlation length was not impacted in the same conditions (Figure 3G). These observations strengthen the hypothesis that coherent chromatin movements do not depend on underlying histone motions, but also on the chromatin structures (*31*) and transcription state (*38*) that may become progressively altered after the direct, local effect of TFs on chromatin. Importantly, our mobility analysis of chromatin is sensitive enough for revealing changes in chromatin reshaping over long ranges. To conclude, these results show that TF overexpression induces progressively coherent chromatin movement changes without a significant change in their diffusive behaviors.

SIX6 directly alters DNA mobility

We next asked whether DNA exhibits the same dynamic response as histones upon chromatin opening or closing. We performed live-cell imaging of DNA labeled by SiR-Hoechst 647(*39*) in the iCDX2 and iSIX6 cell lines, using the same imaging conditions as for H2B-mCherry. Hi-D analysis revealed a modest change in DNA mobility with CDX2 induction, with only one diffusion regime that was slightly increased (Figure 4A). In contrast, a significant increase of *D* for the three populations was detected upon SIX6 expression (Figure 4B) even though SIX6 modulated chromatin accessibility at a smaller number of loci than CDX2. In contrast to H2B motions, the motion models underlying DNA diffusivity following expression of SIX6 were mainly converted from diffusion with directed motion such as DA and DAV to free diffusion (D) and anomalous diffusion (DA) (Figure 4A, B: bottom panels). The increase of free diffusive

motions of DNA might be caused by the loss of DNA-binding proteins complexes involved in transcriptional activity (*31*). Also losing the binding of motor proteins in closed chromatin such as RNA Polymerase and chromatin remodelers may explain the decrease in directed motion (DAV). This interpretation is supported by a decrease in the directional correlation length of DNA by both CDX2 and SIX6 (Figure 4E, F), while magnitudinal correlation length was not changed (Figure 4C, D). Overall, SIX6 markedly alters DNA mobility while CDX2 shows a modest effect on DNA mobility.

The impact of CDX2 on chromatin dynamics is partially mediated by transcriptional activity

We next wondered how much the dynamics response to chromatin opening induced by CDX2 is dependent on downstream changes in transcriptional activity. To address this question, cells treated with dox and either triptolide (TPL) or Actinomycin D (ActD) to halt RNA polymerase (RNA Pol) initiation and elongation, respectively, were compared to cells without dox nor inhibitors. This comparison thus allows us to determine the direct impact of CDX2 and SIX6 on chromatin, without downstream modulation of transcriptional activity that may alter chromatin dynamics. The same H2B-mCherry imaging conditions were applied for both transcription inhibitors. We first performed Hi-D analysis to study chromatin mobility in these conditions. TPL treatment had almost no impact on chromatin mobility, with the *D* value of only one population of H2B slightly increased (Figure 5A). In contrast, ActD treatment resulted in a significant increase in the *D* value of two populations of H2B (Figure 5B). Therefore, the major contribution of transcription to H2B mobility is provided by transcriptional initiation, while transcriptional elongation has a small effect on the global changes in chromatin dynamics. The magnitudinal correlation length of H2B upon both transcription initiation and elongation inhibition decreased to $\xi \approx 1.5$ µm, a decrease of 0.5 µm in comparison to dox-only conditions (Figure 5C). In contrast, the directional correlation length was not changed (Figure 5D). The partial decrease of global H2B mobility during inhibition of transcription elongation by RNA Pol II is in line with transcription-induced constraints on local and global chromatin mobility by tethering RNA polymerase II (RNA Pol II) to chromatin (*32*, *40*, *41*). In conclusion, inhibition of transcription elongation only moderately blocks changes in global chromatin dynamics induced by CDX2.

CDX2 and SIX6 differ in their diffusion but not incoherent movements

We next sought to quantify CDX2 and SIX6 dynamics in the context of their overexpression and chromatin. We thus performed two-color live-cell imaging of H2B-mCherry and CDX2-

YPet or SIX6-YPet. Time-lapse imaging for both TFs and chromatin was acquired after a 24-hour dox incubation, and single-cell Hi-D analysis was used to determine the diffusion behavior of both CDX2 and SIX6 in the context of chromatin opening and closing, respectively (Figure 6 A, B). Hi-D analysis of both CDX2-YPet and SIX6-YPet yielded three-population of diffusion constants for both TFs and chromatin. The *D* values of CDX2 were significantly lower than the *D* values of H2B (Figure 6C top panel). On the other hand, the *D* values of SIX6 were close to the *D* values of H2B (Figure 6D top panel), suggesting that SIX6 stays anchored to DNA in the repressing process. This is consistent with a previous study reporting an increase in dynamics of a repressor TF bound to DNA for chromatin folding (*42*). Interestingly, SIX6 diffusion was twice as fast as CDX2, which might be caused by its binding to initially highly accessible chromatin. In comparison to CDX2, the motion models describing SIX6 diffusivity showed a notable increase in molecules with DA and a decrease of molecules with DV (Figure 6C, D: bottom panels) (see Discussion).

We then quantified the spatial correlation length for both CDX2 and SIX6 in the context of chromatin motion. DFCC analysis yielded identical magnitudinal correlation lengths for both SIX6 and CDX2 (0.5 µm) (Figure 6E, F). These correlated motions of CDX2 over several hundreds of nanometers suggest the formation of domain-like TF clusters, consistent with the described formation of TF condensates (*43*). Interestingly, SIX6 displayed a similar correlation length as chromatin, suggesting a homogeneous mobility distribution of SIX6 within closed chromatin domains. This contrasts with CDX2, for which the magnitudinal correlation length exhibited half of the length of chromatin, with an increase of the directional correlation length (Figure 6G). This suggests that domain-like clusters of CDX2 are spreading over the half of correlated chromatin domains and flow coherently over several µm (Figure 6H). Interestingly, SIX6 and chromatin exhibit identical diffusion constants and magnitudinal correlation lengths values, suggesting that SIX6 constitutes a dynamic complex with DNA (see Discussion).

Discussion

The concept that open and closed chromatin states are correlated to local diffusivity is based on the idea that open chromatin must be dynamic to allow TFs to bind and initiate its remodeling (*6*). The studies that linked chromatin diffusion to function focused mainly on analyzing the mobility of a single gene locus (*44*, *45*) or sparse chromatin loci over the whole-nucleus (*26*, *29*). These approaches, however, did not allow for determining nucleus-wide chromatin dynamics changes in response to TF binding. Also, these studies mainly relied on the observation of high mobility of active chromatin (open) at the nuclear interior and low mobility of heterochromatin (closed) at the nuclear periphery as markers for transcriptional

activities. However, a recent study showed that chromatin dynamics are uncoupled from its compaction, revealing that closed chromatin is also very dynamic (*31*). Also, chromatin-interacting proteins were proposed to coordinate chromatin dynamics over a long range for gene transcription and genome organization (*5*). The dynamic process of opening and closing chromatin and its coordinated motions nucleus-wide in response to TF activity have not been studied. To determine the dynamic response of nucleus-wide chromatin to TF opening or closing chromatin, we combined Hi-D and DFCC methods (*31*, *32*). The combination of both methods accesses the local mobilities of chromatin and TFs in a nucleus-wide manner. They allow the precise classification of the motion model underlying these mobilities and quantify coherent movements of chromatin and chromatin-associated proteins.

To study the impact of an individual TF-mediated local chromatin opening and closing on chromatin dynamics, we chose two TFs with opposite impacts on chromatin accessibility. We used dox-inducible expression in a cell line that does not express CDX2 or SIX6 endogenously (*33*), ensuring that global chromatin dynamics changes are directly caused by TF activity. The overexpression of both TFs induced an increase in the chromatin mobility landscape over a long-range of coordinated movements. While this study does not allow us to directly address the molecular mechanisms underlying these motions, these are compatible with changes in the nucleosome landscape caused by the expression of CDX2 or SIX6. The dislodging of nucleosomes from DNA through chromatin opening can increase global chromatin mobility (*46*, *47*). In general, the increase of *D* emerges from the decrease of molecular friction to establish intramolecular conformational changes (*48*). Particularly, the increase of chromatin motions at enhancers and promoters arising from molecular perturbations is proposed to be caused by the stirring of chromatin domains (*49*) due to a non-thermal molecular motion (*45*). Stirring of chromatin domains may increase the contact frequencies of enhancers and promoters without the formation of stable enhancer-promoter loops and lead to coherent movements of chromatin on a micrometer scale (*50*). In opening chromatin by CDX2, the decrease in the fraction of DA diffusion could be caused by a decrease in the number of trapped histone molecules that explore a volume lower than predicted by free diffusion (*51*). The slight increase in directed motions may result from the recruitment of molecular motor proteins such as chromatin remodelers and RNA Polymerase for remodeling chromatin structure and regulating transcription (*52*, *53*). In contrast, in closed chromatin, the increase in the fraction of DA diffusion trajectories underlying H2B mobility could be attributed to the increase of specific TFs binding to histones that traps more H2Bs in a smaller volume. The decrease of directed motion of H2B combined with an increase of free diffusion of DNA is likely due to the eviction of molecular motor-driven motor proteins bound to histones such as RNA Polymerase (*31*). Our results hint at the contribution of specific protein-DNA binding as

well as motor protein-mediated chromatin mobility in the molecular activities for shaping genome dynamics both for opening and closing chromatin.

We observed a progressive change in magnitudinal correlation length as a function of CDX2 overexpression duration and the partial reversal of the impact of CDX2 on this parameter upon inhibition of transcriptional initiation or elongation. These data are compatible with a scenario that first reflects chromatin opening by pioneer TF activity, while later increases may be caused by downstream effects on transcription (*54*). While opening chromatin is a unidirectional process (Figure 7C), the gradient in directional correlation length in closing chromatin suggests that the chromatin packing process elicits anti-directional movements. This integrated analysis of Hi-D and DFCC indicates that coherent histone motions do not depend only on intrinsic nucleosome dynamics and may depend on TF function and transcriptional state (*38*). The partial decrease of chromatin mobility by transcription elongation inhibition could be due to the tethering of RNA Pol II to DNA in transcription hubs, which hinders chromatin motion (*32*, *40*, *41*). This suggests that the majority of H2B motion changes happen during transcription initiation. This conclusion is supported by the H2B mobility analysis of TPL treated cells, in which the overexpression of CDX2 had almost no impact on chromatin mobility. TPL-transcription factor IIH binding impedes ATP-dependent helicase activities to open DNA for transcription initiation, and thereby decreases gene expression (*55*). Thus, we propose that transcription inhibition by TPL abolishes the stirring of chromatin domains due to a non-thermal molecular motion that prohibits chromatin mobility increase. The proposed molecular stirring model could enhance enhancer–promoter interactions within the local chromatin domain to facilitate transcriptional initiation.

As SIX6 initiates chromatin closing, we hypothesize that it constitutes a dynamic complex of high molecular structure with other co-repressors allowing chromatin compaction. The diffusion of SIX6 in this complex may thus reflect the diffusion of SIX6 attached to chromatin, which is in line with similar SIX6 and H2B diffusion constants. In comparison to CDX2, the fast diffusion of SIX6 in this complex is consistent with higher dynamics of chromatin interacting proteins that are part of complexes, as compared to individual proteins (*42*). Furthermore, the disruption of chromatin structure during the chromatin folding process increases the fraction of diffusing molecules bound to their binding sites in trapped volumes (*56*, *57*), which can explain the increase in the fraction of DA SIX6 molecules. This hypothesis is supported by our results of the identical magnitudinal correlation lengths ($\xi \approx 0.5$ µm) for both H2B and SIX6. Our findings are thus in line with results obtained by simulations that an individual TF enables to connect DNA segments for shaping genome structure (*58*). Also, our experimental results on the role of TFs in shaping the genome mobility landscape are consistent with the *diffusing*

transcription factor model for driving chromosome organization (*37*), which postulates that TFs bound to active and inactive chromatin domains drive chromosome organization by the construction of chromatin-TFs-chromatin bridges (*59*). In this model, specific and nonspecific TFs-chromatin binding to fold chromosomes into loops and topological domains create bridging-induced phase separation and the establishment of TF clusters (*37*, *59*). The multivalent property of TFs allows binding more proteins to bind, producing a thermodynamic (entropic) positive feedback loop that results in the formation of clusters (*60*), which are in the size range of nuclear bodies such as transcriptional condensates (0.3 to 1.0 µm) (*60*, *61*). These TF clusters may explain our coherent domain-like clusters from SIX6 and CDX2 motions detected by DFCC analysis (Figure 6E, F).

The combination of Hi-D and DFCC methods allows studying local and global mobility changes as well as coordinated motion of chromatin dynamics landscape in response to TFs. The quantitative dynamics analysis of chromatin and TFs in their physiological environment provides a biophysical understanding of how chromatin structure responds dynamically to TF functions. This analysis can be a basis for studying the impact of other TFs and chromatin binding proteins on chromatin dynamics for genome organization and gene expression regulation in living cells. It would be interesting to combine these methods with time-resolved super-resolution chromatin imaging (*9*), allowing the full dynamics of both the chromatin state (the motif of TF binding sites) and the 3D structure to be investigated.

Methods

EXPERIMENTAL MODEL AND SUBJECT DETAILS

Cell Culture

NIH-3T3 cell lines stably expressing H2B-mCherry, the rtTA3G transactivator, and TRE3G-controlled (doxycycline (dox)-inducible) CDX2 and SIX6 fused to a yellow fluorescent protein (YPet) (iCDX2 and iSIX6 cell lines, respectively) were used for the experiments (*33*). We also used the parental cell line expressing H2B-mCherry and rtTA3G only as a negative control. Cells were maintained in Dulbecco's modified Eagle's medium (DMEM) (ThermoFisher) supplemented with Glutamax, 2 µg/ml Puromycin (ThermoFisher), and 1% Penicillin-Streptomycin (Bioconept), 10% Fetal bovine serum (ThermoFisher), and 1 mM sodium pyruvate (Sigma-Aldrich) at 37°C with 5% CO2. Cells were grown in 100 mm cell culture dishes and split every other day.

To evaluate the effect of transcription initiation and elongation on chromatin mobility in living cells, 500nM triptolide or 5µg/mL actinomycin D (Sigma-Aldrich) was added to the imaging medium (FluoroBrite DMEM, ThermoFisher) for few minutes before imaging, respectively.

METHOD DETAILS

Live cell Imaging

Live chromatin imaging

Cells were plated for 24h on 35 mm Petri dishes with a #1.5 coverslip-like bottom (µ-Dish, Ibidi) with a density of about 1×10^5 cells/dish. For Dox induction conditions, cells were supplied with 500 ng/ml doxycycline (Sigma-Aldrich) for 24 h before imaging. NIH-3T3 cell lines were labelled with the SiR-DNA (5-610CP-Hoechst) dye (gift from G. Lukinavicius)(*39*). On the day of imaging, SiR-DNA was added to the medium at a final concentration of 1µM and cells were incubated at 37°C for an hour. Cells then were washed gently three times with pre-warmed phosphate-buffered saline (PBS). Before imaging, the medium was changed to FluoroBrite DMEM medium (Thermofisher) containing all medium supplements for live-cell imaging. Live chromatin imaging was acquired using a Spinning Disk CSU W1 (CSU-X1-M1N, Yokogawa) in a 37 °C chamber with controlled humidity and 5% CO2. For H2B-mCherry imaging, a pumped diode laser with a 561 nm wavelength and 50% laser power was used for excitation, and the emission of the mCherry signal was filtered by a bandpass filter ET605/70m (Chroma). For DNA-SiR imaging, a solid-state laser with a 640 nm wavelength and 80 % laser power was used for excitation, and the emission of the SiR–Hoechst was filtered by a single-band bandpass filter (ET700/75m, Chroma. A 100x oil immersion objective (Olympus UPlanSApo) with a 1.4 NA was used for all excitation wavelengths. Videos of 200 frames were acquired using the VisiView software (Visitron) and detected using a sCMOS camera (ORCA-Flash4.0) and (1×1 binning), with a sample pixel size of 65 nm.

Live cell imaging of transcription factor expression dynamics

To determine the temporal dynamics of CDX2-YPet and SIX6-YPet levels after dox induction, the iCDX2 and iSIX6 cell lines were seeded in a 96-well plate. Cells were treated with 500ng/ml of dox to induce expression of either transcription factor for different time durations (6 hrs, 12 hrs, and 24 hrs). Live cell imaging of CDX2-YPet and SIX6-YPet was performed using an IN Cell Analyzer 2200 apparatus (GE Healthcare) with a 20× magnification objective at 37°C and 5% CO2. The YFP fluorescence channel was used for YPet detection. For high-resolution imaging, live imaging of both CDX2-YPet and SIX6-YPet was acquired using a Spinning Disk confocal microscope (CSU W1 (CSU-X1-M1N, Yokogawa) using the same condition as for

live chromatin imaging. A solid-state laser with a 488 nm wavelength and 40 % laser power was used for excitation, and the emission of the YPet was filtered by a single-band bandpass filter (ET525/50m, Chroma).

Image processing and analysis

Drift registration

All analyzed videos were tested for drift. Drift was calculated by the cross-correlation of the first image of the nucleus sequence and every following image of the whole video. Using Gaussian approximation of the correlation peak, the position of the correlation peak was determined with sub-pixel accuracy. Only videos with a drift less than 10 nm were considered for analysis.

Denoising

To denoise the raw images, a non-iterative bilateral filtering procedure was applied to the recorded videos. Rapid transitions from low- to high-intensity areas (e.g., from euchromatin to heterochromatin) were treated with a bilateral filter with a half-size of the Gaussian bilateral filter window of 5 pixels to avoid over-smoothing. Only images with a signal-to-noise ratio (SNR) of 20 dB were considered for the analysis.

Hi-D analysis

The Hi-D method was described in detail in our previous work (*32*), thus here we will only highlight the most important steps for Hi-D analysis. Briefly, Optical Flow was applied to estimate the flow fields (displacement vector) for each pixel of any two consecutive images in an image series (*62*). Flow fields estimated by Optical Flow were interpolated into trajectories of virtual particles, considering every flow field of each pixel represents a virtual molecule. These trajectories are used for MSD analysis for estimating the biophysical properties of chromatin and TFs mobility and motion models that underlie this mobility process.

Mean square displacement (MSD) models

The MSD can be analytically expressed for anomalous diffusion, confined diffusion, and directed motion in two dimensions. Anomalous diffusion was proven to fit chromatin motion more than confined diffusion (*32*), therefore confined diffusion was neglected in our analysis. Also, other forms of motion can show overlaying of two or more of these models, leading to a grouping of anomalous and directed motions. This results in five possible MSD models as follows:

Free diffusion (D) $$MSD_D(\tau) = 4D\tau + o$$

Anomalous diffusion (DA)	$MSD_{DA}(\tau) = 4D_\alpha \tau^\alpha + o$
Drift (V)	$MSD_V(\tau) = v^2\tau^2 + o$
Free diffusion + drift (DV)	$MSD_{DV}(\tau) = 4D\tau + v^2\tau^2 + o$
Anomalous diffusion + drift (DAV)	$MSD_{DAV}(\tau) = 4D_\alpha \tau^\alpha + v^2\tau^2 + o$

where D_α is the diffusion coefficient in units of $\mu m^2/s^\alpha$, α is its anomalous exponent, and $v\,[\mu m/s]$ its velocity. Note that every general diffusion coefficient D_α has different units, corresponding to the specific value of α. For clarity, we mention to it as the diffusion coefficient D through the manuscript. To account for experimental noise, a constant offset o is added to every model.

MSD model selection

We apply a Bayesian inference approach to examine the five motion models for any given MSD curve as explained in (*32*, *63*). The MSD analysis was performed locally by selecting the 3x3 neighborhood of a pixel. This criterion allowed us to identify possible outliers within the interquartile range criterion, and then compute the error covariance matrix of the data within the pixel neighborhood. The constraint to a single pixel and its neighborhood allows performing local MSD analysis of trajectories. The MSD is therefore calculated for every pixel independently, resulting in a space- and time lag-dependent MSD. *D* was calculated out of the fitting of all tested models for all assigned trajectories.

Deconvolution of sub-populations

D values are represented as histograms. Since the diffusion coefficients in our data are not only calculated from the free diffusion model but also from anomalous and drift diffusions, the distribution of diffusion coefficients cannot be expressed analytically for all types of diffusion. Considering that our data set cannot be characterized by a single distribution but by a mixture of distributions, we deconvolve the D values sets by a General Mixture model (GMM), in which each data point is described as a part of a normal or log-normal distribution.

$$f_N(Y|\mu,\sigma^2) = \frac{1}{\sqrt{2\pi}\sigma} e^{-\frac{(Y-\mu)^2}{2\sigma^2}} \quad \text{and}$$

$$f_L(Y|\mu,\sigma^2) = \frac{1}{Y\sqrt{2\pi}s} e^{-\frac{(\ln(Y)-m)^2}{2s^2}},$$

respectively. We count up to three subpopulations, as decided in the original method (*32*), to be detected in our data set, and pattern the total density estimation as an overlap of one, two, or three subpopulations, i.e., the Mixture Model indicates

$$f_{GMM}(Y) = \sum_k w_k\, f_k\left(Y\middle|\mu_k,\sigma_k^2\right)$$

for both normal and log-normal distributions, where the sum goes to 1, 2, or 3. The w_k labels the weights for each population, which fulfill $0 \leq w_k \leq 1$ and compile to unity. The weights of every part are directly proportional to the area of the histogram enclosed by this part and therefore its presence in the data set. The GMM analysis is processed using the *pomegranate* machine learning package for probabilistic modeling (*64*).

We then apply the Bayesian Information Criterion (BIC) to infer the number of subpopulations that are included in the D results represented in a histogram and the spatial distribution model these populations belong to. BIC can therefore evaluate the precision of each model, which is calculated by (*65*)

$$BIC = -2\ln(\hat{L}) + p\ ln(n),$$

where $\hat{L}$ donates the maximum likelihood, p represents the number of parameters in the model and n is the number of data points used for the fit. To assess which model is suitable for our data, we tested all examined models for each histogram and evaluated the ideal model using the BIC. Six models were tested for all histograms as three different populations (1, 2, and 3) for both normal distribution and log-normal distribution. Based on this assessment using the BIC, the *D* results were best described with log-normal distribution and 3 subpopulations. The data points are assigned to fall under each population resulting in slow, intermediate, and fast sub-populations.

DFCC analysis

DFCC also relies on the Optical Flow method to estimate the 2D apparent motion field chromatin motion (*31*). The two-dimensional spatial autocorrelation function $r(\Delta x, \Delta y)$ of a flow field $\gamma(\mathrm{x}, \mathrm{y})$ was calculated for horizontal and vertical space lag by the Fast Fourier Transform as following:

$$r(\Delta x, \Delta y) = \frac{\mathcal{F}^{-1}[\mathcal{F}(\gamma) \cdot \mathcal{F}^{*}(\gamma)]}{\langle\gamma\rangle\langle\gamma\rangle},$$

where $\mathcal{F}^{-1}(\cdot)$ is the inverse Fourier transformation, and $\mathcal{F}^{*}(\cdot)$ is the complex conjugate of the Fourier transformation. The 2D correlation function was projected as a radial average onto one dimension using the space lag $\rho^2 = \Delta x^2 + \Delta y^2$. Thus, the correlation function turns to a function of the space lag only, i.e. $r = r(\rho)$. The correlation curves over space were fitted by the Whittle-Màtern model (*66*):

$$r(\rho) = \frac{2^{1-\nu}}{\Gamma(\nu)}\left(\frac{\rho}{\xi}\right)^{\nu} K_{\nu}\left(\frac{\rho}{\xi}\right).$$

where $\Gamma(\cdot)$ represents the gamma function, $K_\nu(\cdot)$ denotes the modified Bessel function of the second type of order ν, ρ_c denotes the correlation length and ν is the smoothness parameter. Note that ξ denotes both the directional and magnitudinal correlation lengths. Whilst ρ_c characterizes the long-range behavior, the smoothness parameter ν defines the local, high-frequency component of the correlations (a parameter describes the flow field as smooth or rough; large ν means that the underlying spatial process is smooth in space, whereas the process is considered as rough for small ν). These two parameters were averaged for each time interval over all time points. As we did not find significant changes of ν between the different conditions we do not show values for the smoothness parameter.

Relative fluorescence intensity calculation

The images of H2B-mCherry-stained nuclei for different expression time durations (6, 12 and 24 hours) were analyzed with the FIJI software incorporating StarDist 2D (*67*). Briefly, nuclei were segmented using an algorithm based on star-convex polygons. The median intensity and standard deviation values for segmented nuclei were analyzed using FIJI.

QUANTIFICATION AND STATISTICAL ANALYSIS

All calculations including the statistical analysis, except for GMM analysis, were carried out using MATLAB with Image Processing, Signal Processing, and Statistics and Machine Learning Toolboxes. The GMM analysis was performed using Python. All analysis was run on a 64-bit Intel CORE i7 workstation with 64 GB RAM and running Windows 10 Professional. Error bars in our analysis show the standard error of the mean (SEM).

DATA AND SOFTWARE AVAILABILITY

The Hi-D and DFCC codes applied in this study are available in the following GitHub repositories: https://github.com/romanbarth/Hi-D, and https://github.com/romanbarth/DFCC, respectively. The data in this study are accessible upon request from the authors.

Supplemental Information

There is a supplemental file attached to this file.

Acknowledgments

We acknowledge funding from the European Union's Horizon 2020 Research and Innovation Programme under the Marie Skłodowska-Curie grant agreement No. 754462 (Eurotech Postdoc Programme). We thank Grazvydas Lukinavicius for providing the Sir-Hoechst for live

DNA staining. We thank Cédric Deluz for helping with operating the Cell Analyzer machine, Shoujie Sun for sharing a code to mask and quantify single-cell intensities, and Roman Barth for assisting with different analysis codes. We would like to thank the EPFL BioImaging & Optics Core Facility and in particular, Thierry Laroche & Olivier Burri, for their assistance in imaging). We also thank the SCITAS team at EPFL (Mathieu Peybernes) for cluster computing help. Finally, we thank Beat Fierz for critical reading and comments on this manuscript

Author contributions

H.A.S. conceived the project, carried out experimental work, designed the data analysis, performed data analysis, interpreted the results, and wrote the original manuscript draft. D.S. conceived the project, interpreted the results, and wrote the manuscript.

Declaration of Interests

The authors declare that they have no competing interests.

References

1. J. Dekker, L. Mirny, The 3D Genome as Moderator of Chromosomal Communication. *Cell* (2016), , doi:10.1016/j.cell.2016.02.007.
2. S. Wang, J. H. Su, B. J. Beliveau, B. Bintu, J. R. Moffitt, C. T. Wu, X. Zhuang, Spatial organization of chromatin domains and compartments in single chromosomes. *Science (80-.).* **353**, 598–602 (2016).
3. B. van Steensel, E. E. M. Furlong, The role of transcription in shaping the spatial organization of the genome. *Nat. Rev. Mol. Cell Biol.* (2019), , doi:10.1038/s41580-019-0114-6.
4. C. P. Johnstone, N. B. Wang, S. A. Sevier, K. E. Galloway, Understanding and Engineering Chromatin as a Dynamical System across Length and Timescales. *Cell Syst.* (2020), , doi:10.1016/j.cels.2020.09.011.
5. H. A. Shaban, R. Barth, K. Bystricky, Navigating the crowd: visualizing coordination between genome dynamics, structure, and transcription. *Genome Biol.* (2020), , doi:10.1186/s13059-020-02185-y.
6. S. L. Klemm, Z. Shipony, W. J. Greenleaf, Chromatin accessibility and the regulatory epigenome. *Nat. Rev. Genet.* (2019), , doi:10.1038/s41576-018-0089-8.
7. H. Chen, M. Levo, L. Barinov, M. Fujioka, J. B. Jaynes, T. Gregor, Dynamic interplay between enhancer–promoter topology and gene activity. *Nat. Genet.* (2018), , doi:10.1038/s41588-018-0175-z.
8. R. Barth, G. Fourel, H. A. Shaban, Dynamics as a cause for the nanoscale

organization of the genome. *Nucleus*. **11**, 83–98 (2020).

9. R. Barth, K. Bystricky, H. A. Shaban, Coupling chromatin structure and dynamics by live super-resolution imaging. *Sci. Adv.* **6** (2020), doi:10.1126/sciadv.aaz2196.
10. I. Berest, C. Arnold, A. Reyes-Palomares, G. Palla, K. D. Rasmussen, H. Giles, P. M. Bruch, W. Huber, S. Dietrich, K. Helin, J. B. Zaugg, Quantification of Differential Transcription Factor Activity and Multiomics-Based Classification into Activators and Repressors: diffTF. *Cell Rep.* (2019), doi:10.1016/j.celrep.2019.10.106.
11. A. Soufi, M. F. Garcia, A. Jaroszewicz, N. Osman, M. Pellegrini, K. S. Zaret, Pioneer transcription factors target partial DNA motifs on nucleosomes to initiate reprogramming. *Cell* (2015), doi:10.1016/j.cell.2015.03.017.
12. K. S. Zaret, J. S. Carroll, Pioneer transcription factors: Establishing competence for gene expression. *Genes Dev.* (2011), , doi:10.1101/gad.176826.111.
13. M. Iwafuchi-Doi, K. S. Zaret, Cell fate control by pioneer transcription factors. *Dev.* (2016), doi:10.1242/dev.133900.
14. S. A. Lambert, A. Jolma, L. F. Campitelli, P. K. Das, Y. Yin, M. Albu, X. Chen, J. Taipale, T. R. Hughes, M. T. Weirauch, The Human Transcription Factors. *Cell* (2018), , doi:10.1016/j.cell.2018.01.029.
15. M. Iurlaro, M. B. Stadler, F. Masoni, Z. Jagani, G. G. Galli, D. Schübeler, Mammalian SWI/SNF continuously restores local accessibility to chromatin. *Nat. Genet.* (2021), doi:10.1038/s41588-020-00768-w.
16. E. T. Friman, C. Deluz, A. C. A. Meireles-Filho, S. Govindan, V. Gardeux, B. Deplancke, D. M. Suter, Dynamic regulation of chromatin accessibility by pluripotency transcription factors across the cell cycle. *Elife* (2019), doi:10.7554/eLife.50087.
17. S. Schick, S. Grosche, K. E. Kohl, D. Drpic, M. G. Jaeger, N. C. Marella, H. Imrichova, J. M. G. Lin, G. Hofstätter, M. Schuster, A. F. Rendeiro, A. Koren, M. Petronczki, C. Bock, A. C. Müller, G. E. Winter, S. Kubicek, Acute BAF perturbation causes immediate changes in chromatin accessibility. *Nat. Genet.* (2021), doi:10.1038/s41588-021-00777-3.
18. S. Berry, C. Dean, M. Howard, Slow Chromatin Dynamics Allow Polycomb Target Genes to Filter Fluctuations in Transcription Factor Activity. *Cell Syst.* (2017), doi:10.1016/j.cels.2017.02.013.
19. J. Chen, Z. Zhang, L. Li, B. C. Chen, A. Revyakin, B. Hajj, W. Legant, M. Dahan, T. Lionnet, E. Betzig, R. Tjian, Z. Liu, Single-molecule dynamics of enhanceosome assembly in embryonic stem cells. *Cell*. **156**, 1274–1285 (2014).
20. H. Liu, P. Dong, M. S. Ioannou, L. Li, J. Shea, H. A. Pasolli, J. B. Grimm, P. K. Rivlin, L. D. Lavis, M. Koyama, Z. Liu, Visualizing long-term single-molecule dynamics in vivo by stochastic protein labeling. *Proc. Natl. Acad. Sci.* **115**, 343–348 (2018).

21. J. C. M. Gebhardt, D. M. Suter, R. Roy, Z. W. Zhao, A. R. Chapman, S. Basu, T. Maniatis, X. S. Xie, Single-molecule imaging of transcription factor binding to DNA in live mammalian cells. *Nat. Methods*. **10**, 421–6 (2013).
22. A. S. Hansen, I. Pustova, C. Cattoglio, R. Tjian, X. Darzacq, CTCF and cohesin regulate chromatin loop stability with distinct dynamics. *Elife* (2017), doi:10.7554/elife.25776.
23. B. T. Donovan, A. Huynh, D. A. Ball, H. P. Patel, M. G. Poirier, D. R. Larson, M. L. Ferguson, T. L. Lenstra, Live-cell imaging reveals the interplay between transcription factors, nucleosomes, and bursting. *EMBO J.* (2019), doi:10.15252/embj.2018100809.
24. A. P. Popp, J. Hettich, J. C. M. Gebhardt, Altering transcription factor binding reveals comprehensive transcriptional kinetics of a basic gene. *Nucleic Acids Res.* (2021), doi:10.1093/nar/gkab443.
25. D. M. Suter, Transcription Factors and DNA Play Hide and Seek. *Trends Cell Biol.* (2020), , doi:10.1016/j.tcb.2020.03.003.
26. J. Lerner, P. A. Gomez-Garcia, R. L. McCarthy, Z. Liu, M. Lakadamyali, K. S. Zaret, Two-Parameter Mobility Assessments Discriminate Diverse Regulatory Factor Behaviors in Chromatin. *Mol. Cell* (2020), doi:10.1016/j.molcel.2020.05.036.
27. M. H. Hauer, S. M. Gasser, Chromatin and nucleosome dynamics in DNA damage and repair. *Genes Dev.* (2017), , doi:10.1101/gad.307702.117.
28. A. A. Agbleke, A. Amitai, J. D. Buenrostro, A. Chakrabarti, L. Chu, A. S. Hansen, K. M. Koenig, A. S. Labade, S. Liu, T. Nozaki, S. Ovchinnikov, A. Seeber, H. A. Shaban, J. H. Spille, A. D. Stephens, J. H. Su, D. Wadduwage, Advances in Chromatin and Chromosome Research: Perspectives from Multiple Fields. *Mol. Cell* (2020), , doi:10.1016/j.molcel.2020.07.003.
29. T. Nozaki, R. Imai, M. Tanbo, R. Nagashima, S. Tamura, T. Tani, Dynamic Organization of Chromatin Domains Revealed by Super-Resolution Live-Cell Imaging. *Mol. Cell*. **10**, 1–12 (2017).
30. H. A. Shaban, A. Seeber, Monitoring the spatio-temporal organization and dynamics of the genome. *Nucleic Acids Res.* (2020), doi:10.1093/nar/gkaa135.
31. H. A. Shaban, R. Barth, K. Bystricky, Formation of correlated chromatin domains at nanoscale dynamic resolution during transcription. *Nucleic Acids Res.* **46**, e77 (2018).
32. H. A. Shaban, R. Barth, L. Recoules, K. Bystricky, Hi-D: nanoscale mapping of nuclear dynamics in single living cells. *Genome Biol.* **21**, 95 (2020).
33. M. Raccaud, E. T. Friman, A. B. Alber, H. Agarwal, C. Deluz, T. Kuhn, J. C. M. Gebhardt, D. M. Suter, Mitotic chromosome binding predicts transcription factor properties in interphase. *Nat. Commun.* (2019), doi:10.1038/s41467-019-08417-5.

34. D. Strumpf, C. A. Mao, Y. Yamanaka, A. Ralston, K. Chawengsaksophak, F. Beck, J. Rossant, Cdx2 is required for correct cell fate specification and differentiation of trophectoderm in the mouse blastocyst. *Development* (2005), doi:10.1242/dev.01801.
35. E. J. Stringer, I. Duluc, T. Saandi, I. Davidson, M. Bialecka, T. Sato, N. Barker, H. Clevers, C. A. Pritchard, D. J. Winton, N. A. Wright, J. N. Freund, J. Deschamps, F. Beck, Cdx2 determines the fate of postnatal intestinal endoderm. *Development* (2012), doi:10.1242/dev.070722.
36. J. P. Kumar, The sine oculis homeobox (SIX) family of transcription factors as regulators of development and disease. *Cell. Mol. Life Sci.* (2009), , doi:10.1007/s00018-008-8335-4.
37. C. A. Brackley, S. Taylor, A. Papantonis, P. R. Cook, D. Marenduzzo, Nonspecific bridging-induced attraction drives clustering of DNA-binding proteins and genome organization. *Proc. Natl. Acad. Sci.* **110**, E3605–E3611 (2013).
38. R. Barth, H. A. Shaban, Spatially coherent diffusion of human RNA Pol II depends on transcriptional state rather than chromatin motion. *bioRxiv* (2022), doi:10.1101/2022.01.19.476954.
39. J. Bucevičius, J. Keller-Findeisen, T. Gilat, S. W. Hell, G. Lukinavičius, Rhodamine-Hoechst positional isomers for highly efficient staining of heterochromatin. *Chem. Sci.* (2019), doi:10.1039/c8sc05082a.
40. T. Germier, S. Kocanova, N. Walther, A. Bancaud, H. A. Shaban, H. Sellou, A. Z. Politi, J. Ellenberg, F. Gallardo, K. Bystricky, Real-Time Imaging of a Single Gene Reveals Transcription-Initiated Local Confinement. *Biophys. J.* **113**, 1383–1394 (2017).
41. R. Nagashima, K. Hibino, S. S. Ashwin, M. Babokhov, S. Fujishiro, R. Imai, T. Nozaki, S. Tamura, T. Tani, H. Kimura, M. Shribak, M. T. Kanemaki, M. Sasai, K. Maeshima, Single nucleosome imaging reveals loose genome chromatin networks via active RNA polymerase II. *J. Cell Biol.* (2019), doi:10.1083/jcb.201811090.
42. A. S. Hansen, I. Pustova, C. Cattoglio, R. Tjian, X. Darzacq, CTCF and cohesin regulate chromatin loop stability with distinct dynamics. *Elife* (2017), doi:10.7554/eLife.25776.
43. A. J. M. Wollman, S. Shashkova, E. G. Hedlund, R. Friemann, S. Hohmann, M. C. Leake, Transcription factor clusters regulate genes in eukaryotic cells. *Elife* (2017), doi:10.7554/eLife.27451.
44. T. Germier, A. Sylvain, K. Silvia, L. David, B. Kerstin, Real-time imaging of specific genomic loci in eukaryotic cells using the ANCHOR DNA labelling system. *Methods* (2018), doi:10.1016/j.ymeth.2018.04.008.
45. B. Gu, T. Swigut, A. Spencley, M. R. Bauer, M. Chung, T. Meyer, J. Wysocka,

Transcription-coupled changes in nuclear mobility of mammalian cis-regulatory elements. *Science (80-.).*, 1–9 (2018).

46. F. R. Neumann, V. Dion, L. R. Gehlen, M. Tsai-Pflugfelder, R. Schmid, A. Taddei, S. M. Gasser, Targeted INO80 enhances subnuclear chromatin movement and ectopic homologous recombination. *Genes Dev.* (2012), doi:10.1101/gad.176156.111.
47. J. Poli, S. M. Gasser, M. Papamichos-Chronakis, The INO80 remodeller in transcription, replication and repair. *Philos. Trans. R. Soc. B Biol. Sci.* (2017), , doi:10.1098/rstb.2016.0290.
48. A. Soranno, B. Buchli, D. Nettels, R. R. Cheng, S. Müller-Späth, S. H. Pfeil, A. Hoffmann, E. A. Lipman, D. E. Makarov, B. Schuler, Quantifying internal friction in unfolded and intrinsically disordered proteins with single-molecule spectroscopy. *Proc. Natl. Acad. Sci. U. S. A.* (2012), doi:10.1073/pnas.1117368109.
49. S. C. Weber, A. J. Spakowitz, J. A. Theriot, Nonthermal ATP-dependent fluctuations contribute to the in vivo motion of chromosomal loci. *Proc. Natl. Acad. Sci. U. S. A.* (2012), doi:10.1073/pnas.1119505109.
50. A. Zidovska, The self-stirred genome: large-scale chromatin dynamics, its biophysical origins and implications. *Curr. Opin. Genet. Dev.* (2020), , doi:10.1016/j.gde.2020.03.008.
51. M. J. Saxton, Diffusion of DNA-Binding Species in the Nucleus: A Transient Anomalous Subdiffusion Model. *Biophys. J.* **118**, 2151–2167 (2020).
52. D. Saintillan, M. J. Shelley, A. Zidovska, Extensile motor activity drives coherent motions in a model of interphase chromatin. *Proc. Natl. Acad. Sci. U. S. A.* (2018), doi:10.1073/pnas.1807073115.
53. N. Gamarra, G. J. Narlikar, Collaboration through chromatin: motors of transcription and chromatin structure. *J. Mol. Biol.* (2021), , doi:10.1016/j.jmb.2021.166876.
54. D. R. Larson, C. Fritzsch, L. Sun, X. Meng, D. S. Lawrence, R. H. Singer, Direct observation of frequency modulated transcription in single cells using light activation. *Elife*. **2013** (2013), doi:10.7554/eLife.00750.
55. O. Bensaude, Inhibiting eukaryotic transcription: Which compound to choose? How to evaluate its activity? *Transcription* (2011), doi:10.4161/trns.2.3.16172.
56. M. J. Saxton, A biological interpretation of transient anomalous subdiffusion. I. Qualitative model. *Biophys. J.* (2007), doi:10.1529/biophysj.106.092619.
57. M. Platani, I. Goldberg, A. I. Lamond, J. R. Swedlow, Cajal body dynamics and association with chromatin are ATP-dependent. *Nat. Cell Biol.* (2002), doi:10.1038/ncb809.
58. H. G. Schmidt, S. Sewitz, S. S. Andrews, K. Lipkow, An Integrated Model of Transcription Factor Diffusion Shows the Importance of Intersegmental Transfer and

Quaternary Protein Structure for Target Site Finding. *PLoS One*. **9**, e108575 (2014).
59. C. A. Brackley, J. Johnson, S. Kelly, P. R. Cook, D. Marenduzzo, Simulated binding of transcription factors to active and inactive regions folds human chromosomes into loops, rosettes and topological domains. *Nucleic Acids Res.* **44**, 3503–3512 (2016).
60. C. A. Brackley, B. Liebchen, D. Michieletto, F. Mouvet, P. R. Cook, D. Marenduzzo, Ephemeral Protein Binding to DNA Shapes Stable Nuclear Bodies and Chromatin Domains. *Biophys. J.* (2017), doi:10.1016/j.bpj.2017.01.025.
61. Y. S. Mao, B. Zhang, D. L. Spector, Biogenesis and function of nuclear bodies. *Trends Genet.* (2011), , doi:10.1016/j.tig.2011.05.006.
62. D. Sun, S. Roth, M. J. Black, A quantitative analysis of current practices in optical flow estimation and the principles behind them. *Int. J. Comput. Vis.* **106**, 115–137 (2014).
63. N. Monnier, S.-M. Guo, M. Mori, J. He, P. Lénárt, M. Bathe, Bayesian approach to MSD-based analysis of particle motion in live cells. *Biophys. J.* **103**, 616–26 (2012).
64. J. Schreiber, Pomegranate: fast and flexible probabilistic modeling in python (2017).
65. G. Schwarz, Estimating the Dimension of a Model. *Ann. Stat.* **6**, 461–464 (1978).
66. B. Matérn, *Spatial variation* (Springer-Verlag, 1986).
67. U. Schmidt, M. Weigert, C. Broaddus, G. Myers, in *Lecture Notes in Computer Science (including subseries Lecture Notes in Artificial Intelligence and Lecture Notes in Bioinformatics)* (2018).

Figure captions

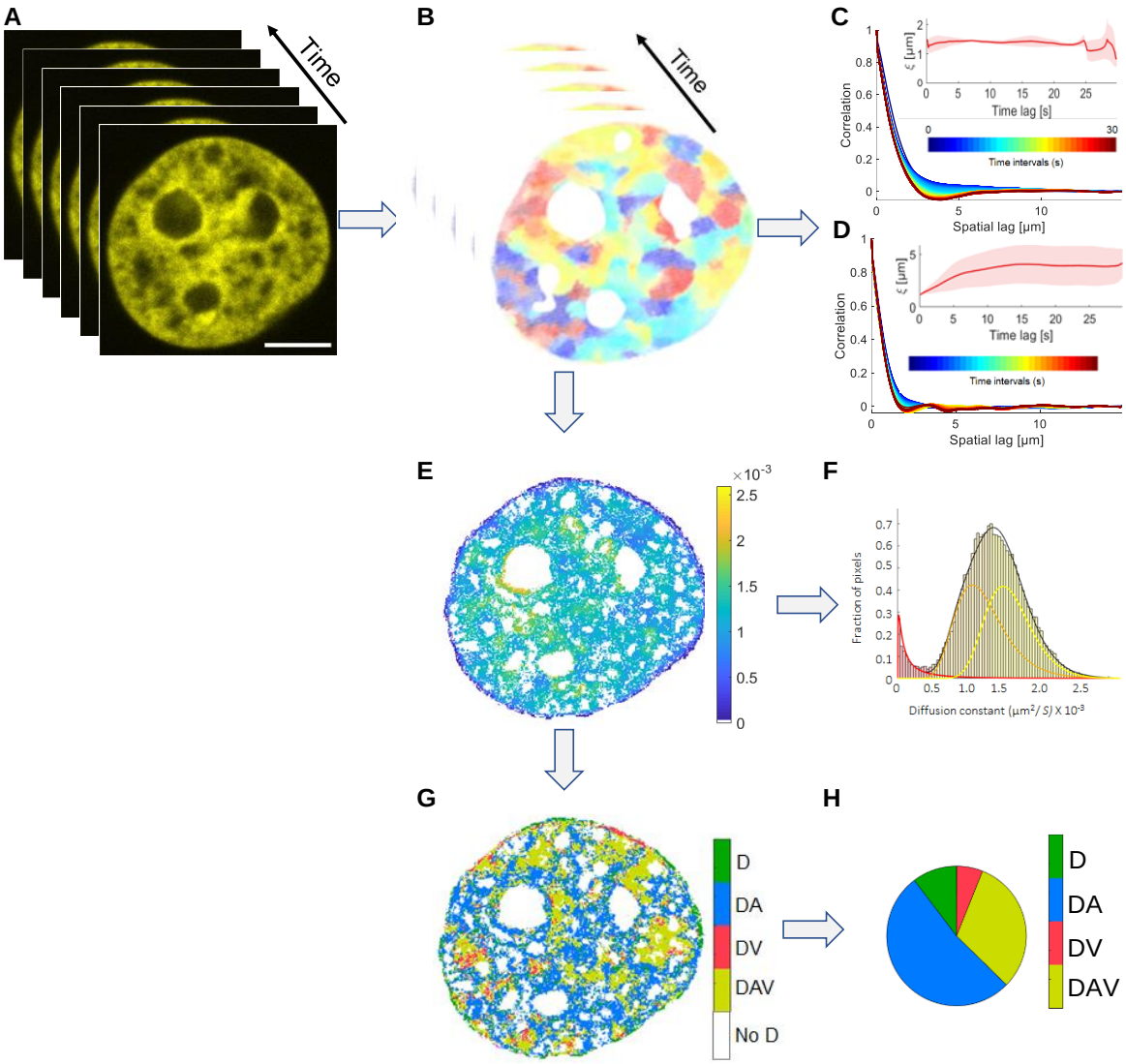

Figure 1. Combination of the Hi-D and DFCC workflows. **A)** H2B-RFP-stained nuclei of NIH-3T3 fibroblast cells were imaged with a time interval of Δt. **B)** Flow fields between successive images were computed using Optical Flow. **C)** The spatial correlation in flow field magnitude (first panel) and **D)** flow magnitude direction (second panel) was computed over increasing space lags (averaged over the two spatial dimensions) and over accessible time lags (from blue to red). Spatial directional and magnitudinal correlation lengths were obtained via regression to the Whittle–Matérn covariance model for every time lag (insets).

The displacement vectors are estimated as in (**B**) and connected over time to generate trajectories of each pixel. The MSD was calculated, followed by Bayesian analysis to determine the motion type for each trajectory. **E-H)** Nucleus-wide motion analysis map using Hi-D. **E)** A map of diffusion constant (*D)* extracted from the best describing model per pixel reveals the local dynamic behaviour of H2B. The unit of the heat map scale is $\mu m^2/S$. **F)** A histogram distribution of D values of the entire nucleus was deconvolved using a general mixture model. **G)** The spatial distribution of the selected models (free diffusion (D), anomalous diffusion (DA), directed motion involving a drift velocity (V), a free diffusion with directed motion (DV), and anomalous diffusion with directed motion (DAV)) for each pixel is shown as a color map. **H)** Pie chart representation of the selected motion models percentage.

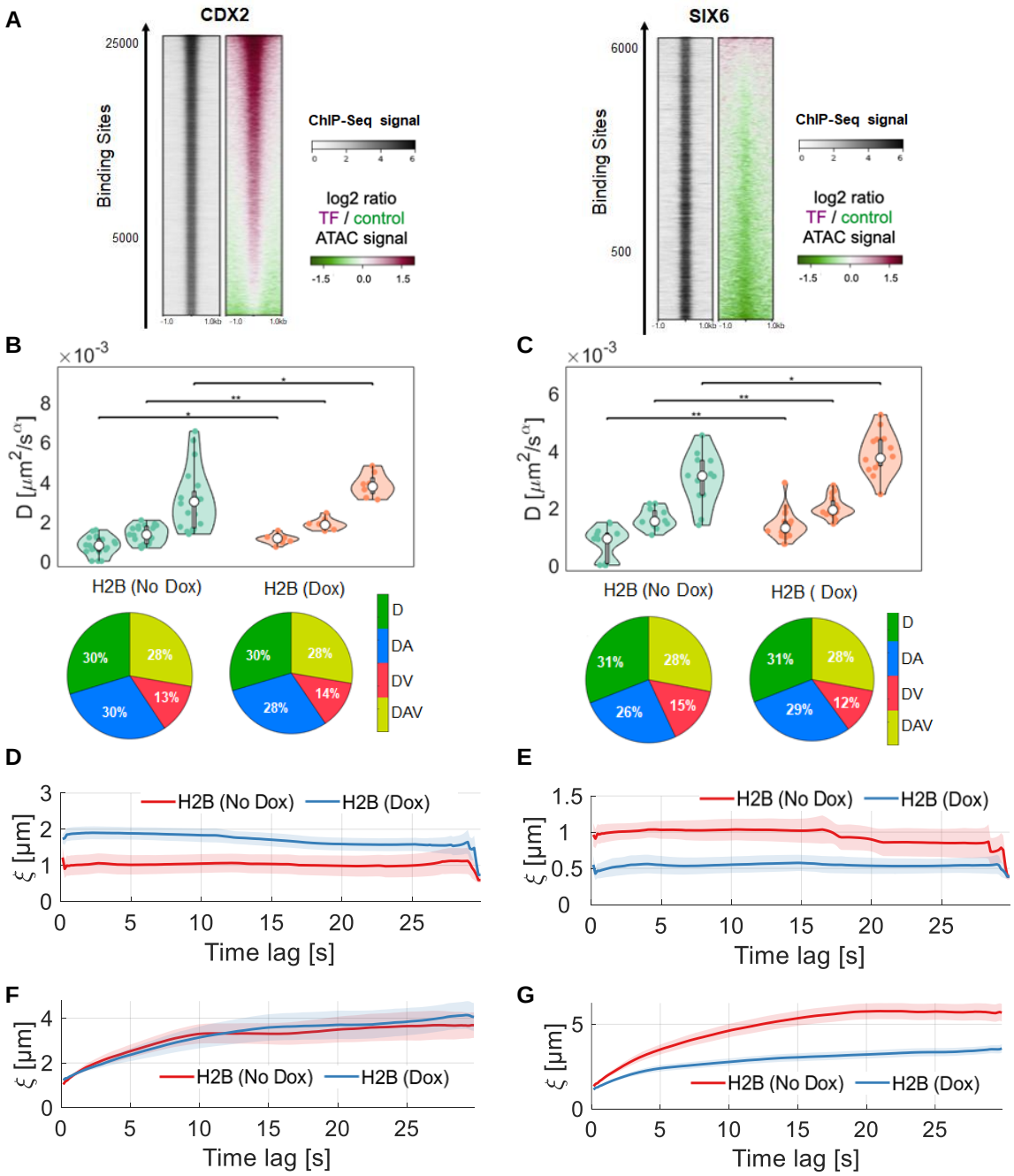

Figure 2. Comparison between the impact of CDX2 and SIX6 on dynamic properties of opening and closing chromatin. **A)** Heatmaps for both ChIP-seq (left) and log2 ratio of ATAC-seq signals of TFs over-expression and control (right) are plotted against the number of binding sites of each TF. The peaks of CDX2 (left panel) and SIX6 (left panel) are 1 kb around the center of ChIP-seq peaks. **B)** Violin plots of the mean diffusion constant of H2B for the three sub-populations mobility groups in control (without Dox induction; $n = 20$), and over-expression of CDX2 TF (with Dox; $n = 20$) cells. **C** as **B** but for SIX6 TF. Statistical significance was assessed by a Friedman test (*$p < 0.05$, **$p < 0.01$, ***: $p < 0.001$). Pie charts of the type of diffusion models on the cell volume for control (no Dox), and CDX2 over-expression (with Dox). The diffusion models are color-coded for the chosen motion

type. **D)** Magnitudinal and **E)** Directional correlation lengths of H2B dynamics in control (without Dox induction), and over-expression of CDX2 TF over increasing time lag. The correlation lengths were averaged for each time interval overall accessible time points. **F** and **G** as **D** and **E** but for SIX6 TF.

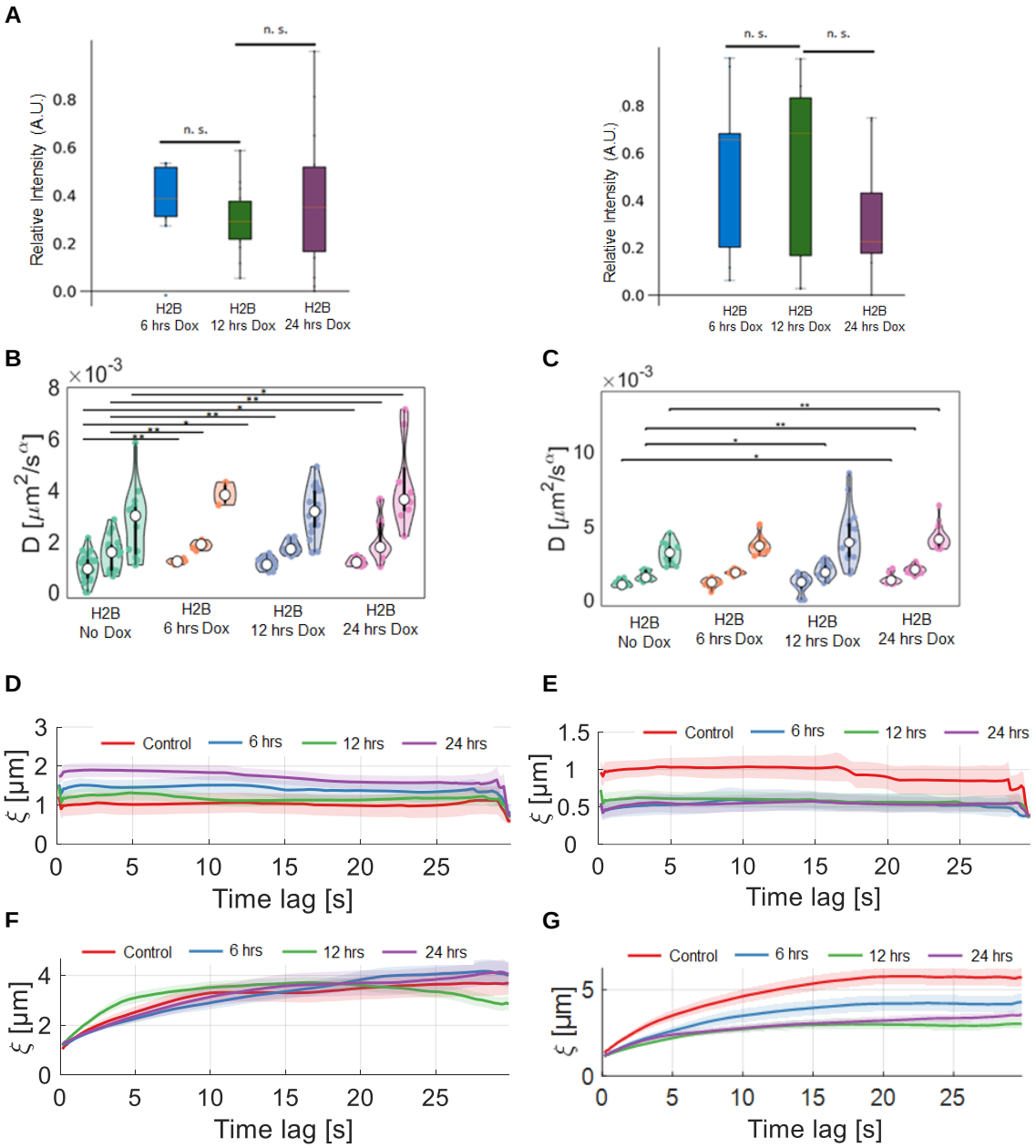

Figure 3. The effect of the expression time length on the coherent movement of chromatin for opening and closing chromatin. **A)** Relative fluorescence intensity of H2B-mCherry-stained nuclei of NIH-3T3 fibroblast cells for different expression time lengths (6, 12, and 24 hours) of CDX2 (left panel) and SIX6 (right panel). The total intensity was normalized by the maximum intensity overall conditions. The median value is shown in red. **B-C)** Violin plots of

the mean diffusion constant of H2B for the three sub-populations mobility groups in control (no Dux induction) and over three different Dox induction time lengths (6, 12 and 24 hours) of CDX2 (B) or SIX6 (C). Statistical significance was assessed by a Friedman test (*$p < 0.05$, **$p < 0.01$, ***: $p < 0.001$). Pie charts of the type of diffusion models on the cell volume for control (no Dox), and CDX2 over-expression (with Dox). The diffusion models are color-coded for the chosen motion type. Numbers are in percent. **D)** Directional and **E)** Magnitudinal correlation lengths of H2B dynamics in control (without Dox induction), and after 6, 12, and 24 hours of Dox induction for CDX2 over increasing time lags. The correlation lengths were averaged for each time interval overall accessible time points. **F** and **G** as **D** and **E** but for SIX6 TF.

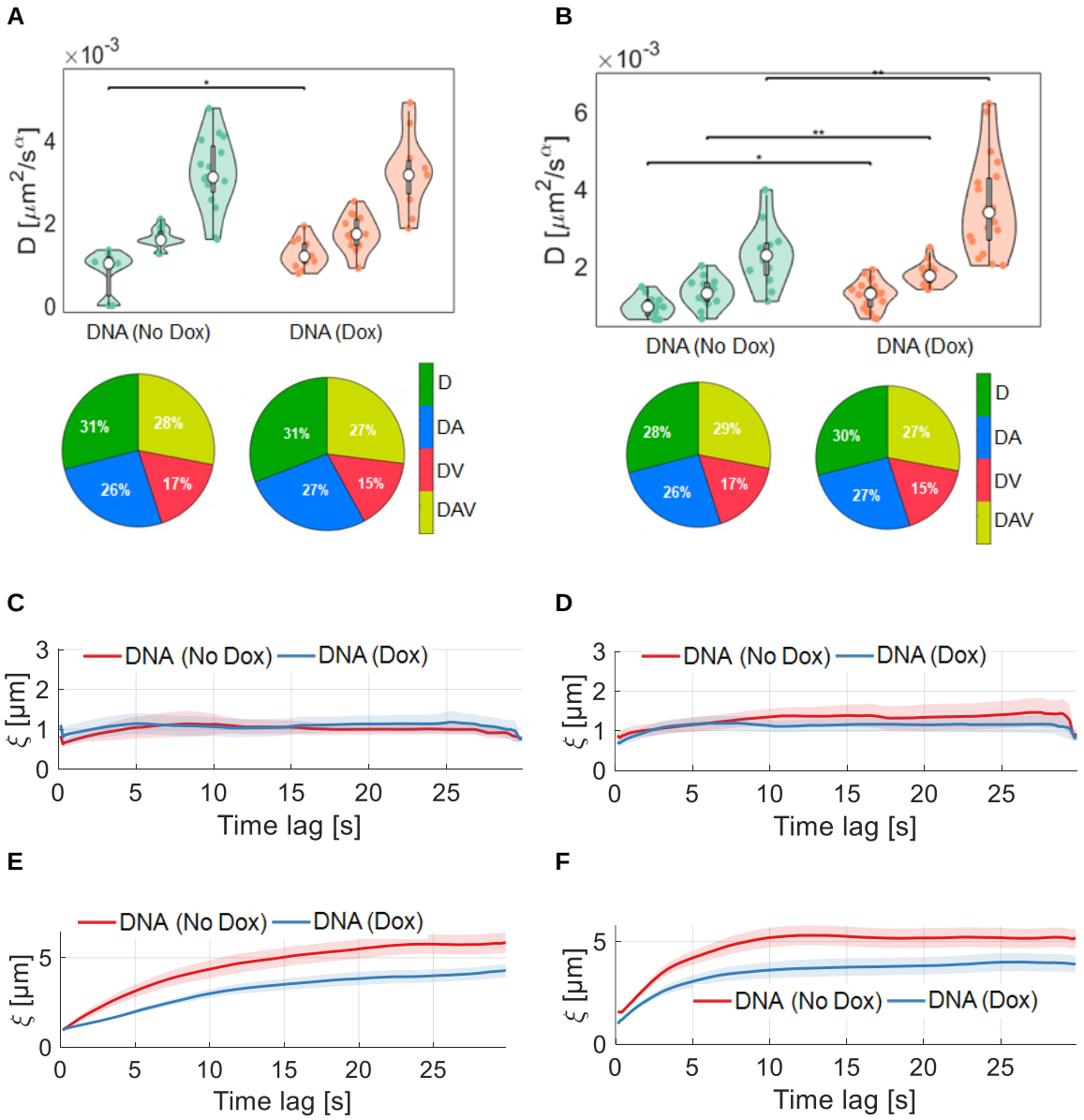

Figure 4. DNA dynamic properties response to expression of CDX2 and SIX6.**A)** Violin plots of the mean diffusion constant of DNA-SiR-647-stained nuclei of iCDX2 cells for the three sub-populations mobility groups without Dox induction ($n = 22$), and with Dox ($n = 19$) cells. **B** as **A** but for SIX6; for the same condition without Dox induction ($n = 22$), and with Dox ($n = 31$) cells. Statistical significance was assessed by a Friedman test (*$p < 0.05$, **$p < 0.01$, ***: $p < 0.001$). Pie charts of the type of diffusion models on the cell volume for control (no Dox), and CDX2 overexpression (with Dox). The diffusion models are color-coded for the chosen motion type. Numbers are in percent. **C and E)** Directional and **D-F)** Magnitudinal correlation lengths of DNA dynamics in control (without Dox induction), and over-expression of CDX2 (C-D) or SIX6 (E-F) over increasing time lags. The correlation lengths were averaged for each time interval overall accessible time points.

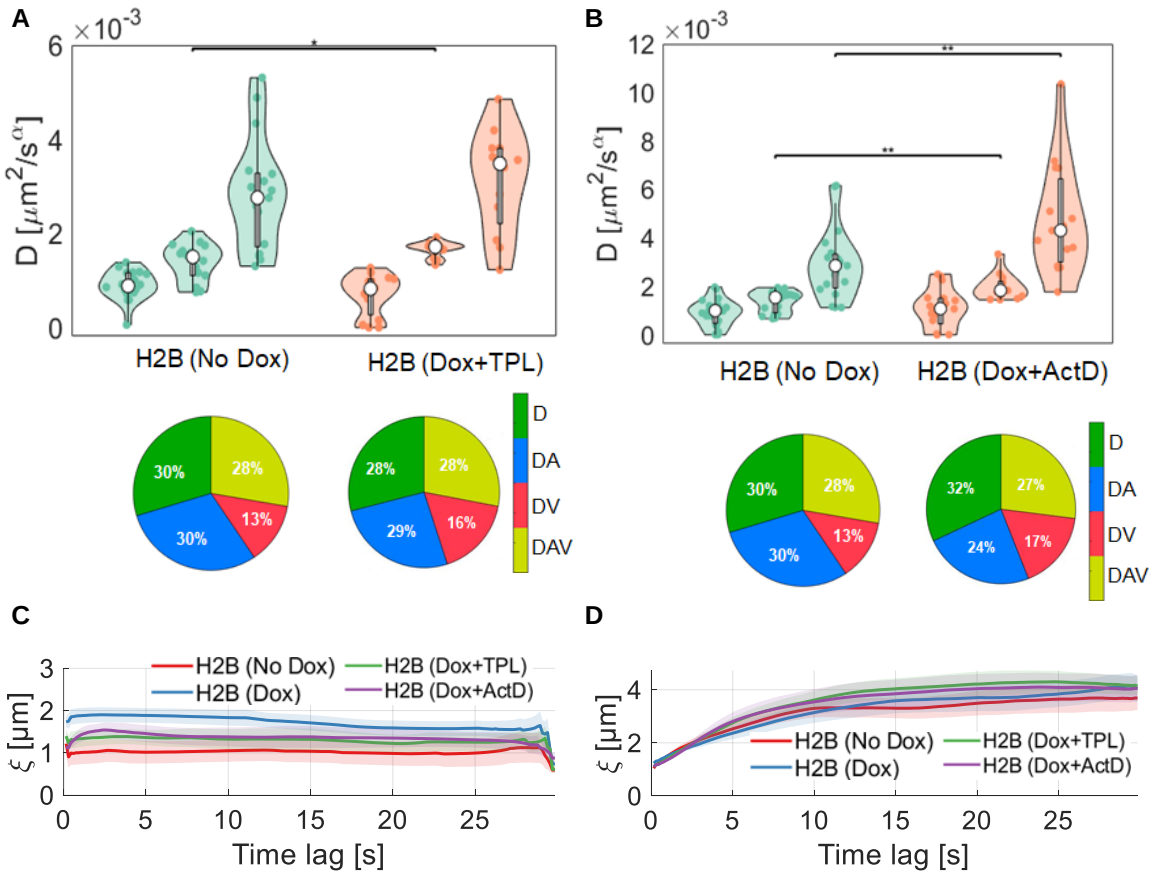

Figure 5. The consequence of transcription initiation or elongation inhibition on the response of dynamic properties to the pioneering activities of CDX2. **A)** Violin plots of the mean diffusion constant for the three sub-populations mobility groups without dox ($n = 20$), or with dox in iCDX2 cells upon treatment with TPL ($n = 16$), and **B)** ActD ($n = 20$) for transcription initiation and elongation inhibition, respectively. Statistical significance was assessed by a Friedman test (*$p < 0.05$, **$p < 0.01$, ***: $p < 0.001$). Pie charts of the type of diffusion models

on the cell volume without or with dox and TPL or ActD in iCDX2 cells. The diffusion models are color-coded for the chosen motion type. **C)** Directional and **D)** Magnitudinal correlation lengths of H2B dynamics in control without or with dox in iCDX2 cells over increasing time lags. The correlation lengths were averaged for each time interval overall accessible time points.

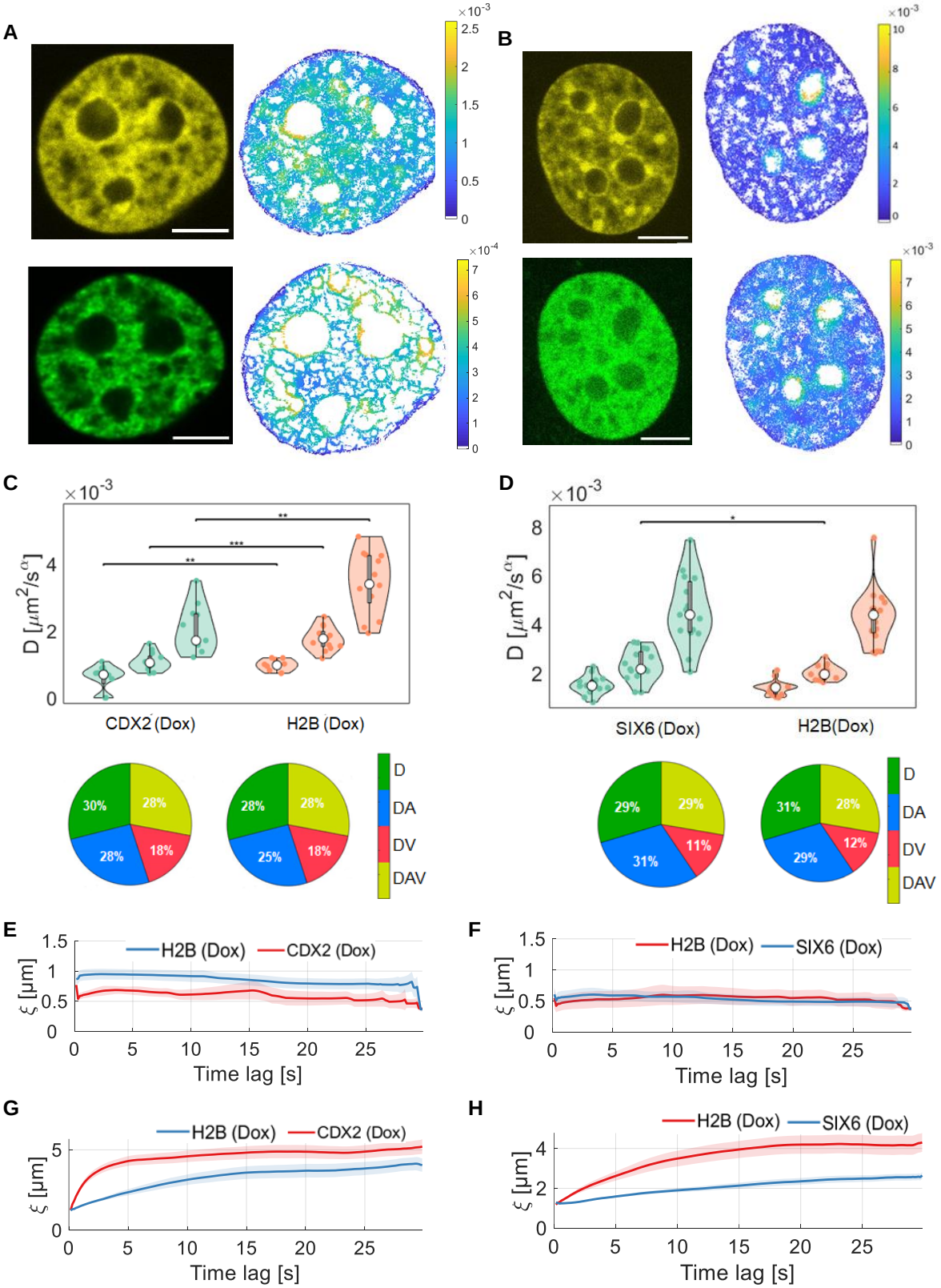

Figure 6. Dynamic properties of CDX2 and SIX6. **A-B)** Example of two-color single live-cell imaging of H2B-mCherry with CDX2-YPet (A) or SIX6-YPet (B) in NIH-3T3 fibroblast cells (left). Scale bar: 3µm. Diffusion constants of spatially mapped onto the nucleus of H2B molecules with both CDX2 cells (right) for the same nucleus. **C-D)** Violin plots of the mean

diffusion constant of H2B-mCherry and CDX2-YPet ($n = 17$) **(C)** or SIX6 (D) stained nuclei ($n = 17$) for the three sub-populations mobility groups in iCDX2 cells treated with dox ($n = 20$) cells. **D)** as **C)** but for SIX6. Statistical significance was assessed by a Friedman test (*$p < 0.05$, **$p < 0.01$, ***: $p < 0.001$). Pie charts of the type of diffusion models on the cell volume for H2B and CDX2 (both with 24 hrs Dox induction). **E and G)** Directional and **F and H)** Magnitudinal correlation lengths of H2B dynamics in control (without Dox induction), and over-expression of CDX2 (E-F) or SIX6 (G-H) over increasing time lag. The correlation lengths were averaged for each time interval overall accessible time points.

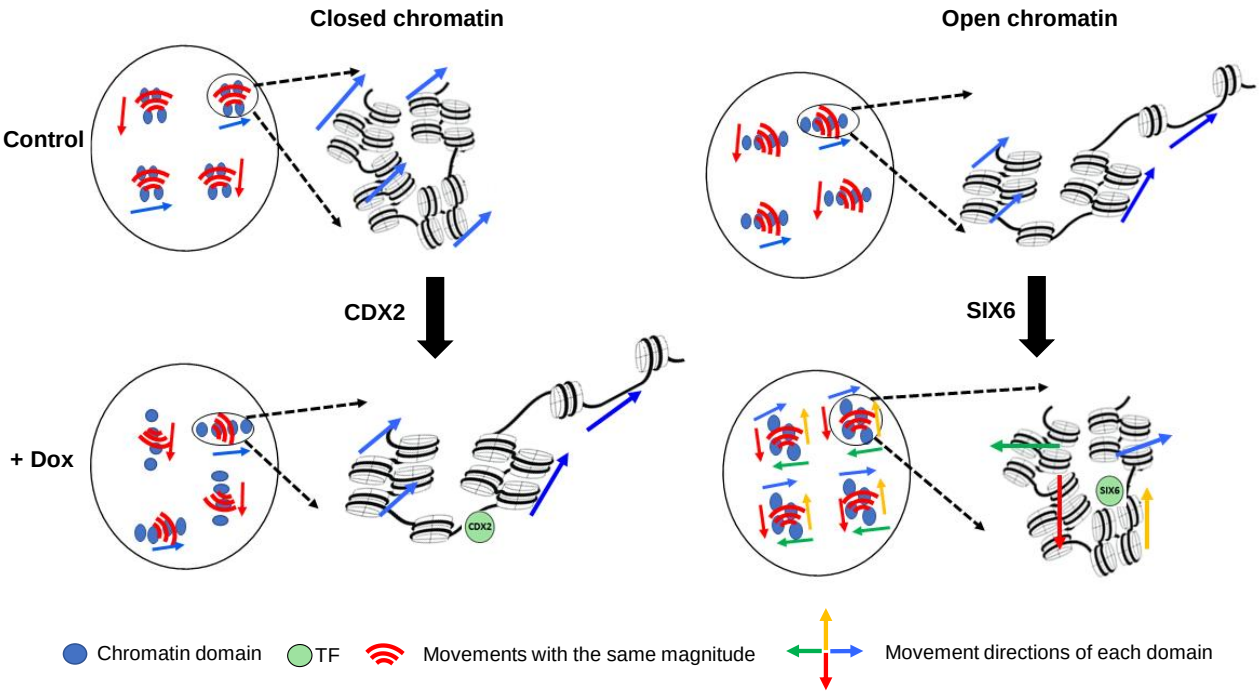

Figure 7. Model of the dynamic response of chromatin structure opening and closing. Representation of chromatin domains (represented by blue spheres) dynamics organization over the entire nucleus as a control for cells without CDX2 or SIX6 expression. Chromatin domains have coordinated movements with the same magnitude (red Wi-Fi symbol) and directions (arrows are color-coded) over spatial distances at the micron scale. Groups of chromatin domains with the same Wi-Fi symbol directionality have the same magnitudinal correlation length. Magnification of a domain illustrates how a chromatin fiber dynamically organizes before TF expression in closed and open chromatin regions. CDX2 expression for opening chromatin by Dox treatment induces an increase in the magnitudinal correlation length of open chromatin domains in a unidirectional process. Bottom: representations of the dynamic organization of chromatin in the presence of CDX2 or SIX6 (green circles). While CDX2 induces unidirectional motions of opened chromatin domains, SIX6 induces multidirectional motions of closed chromatin with shorter magnitudinal correlation length.